MATERIALS CHEMISTRY FRONTIERS

RESEARCH ARTICLE

View Article Online
View Journal | View Issue

Cite this: *Mater. Chem. Front.*, 2022, **6**, 973

A cucurbit[6]uril-carbon dot system: a potentially new bioimaging agent†

Shuai Zhang,[a] Yan Tian,[a] Ming Liu,[a] Tie Hong-Meng,[b] Chun-Rong Li,[b] Xi Zeng, *[a] Xin Xiao [a] and Carl Redshaw *[c]

Received 7th January 2022,
Accepted 28th February 2022

DOI: 10.1039/d2qm00022a

rsc.li/frontiers-materials

We report novel cucurbit[6]uril (Q[6])/carbon quantum dots (CQDs) prepared by solvothermal and nitrogen doped methods. The *m*-Q[6]-CQDs have been characterized by FTIR, XRD and X-ray photoelectron spectroscopy. The obtained *m*-Q[6]-CQDs exhibit good water dispersibility, photostability and strong blue fluorescence emission. The *m*-Q[6]-CQDs also showed good selectivity for metal ions. When Hg^{2+} is present, the fluorescence is quenched, but upon the addition of Al^{3+}, the fluorescence is enhanced. It was also shown that the fluorescence of the *m*-Q[6]-CQDs can resist both the interference from other metal ions as well as high ionic strength environments. The *m*-Q[6]-CQDs were utilized for the optical bioimaging of human prostate cancer (PC-3) cells, and were found to exhibit both low cytotoxicity and excellent biocompatibility.

1. Introduction

Heavy metal pollution is one of the many pollutions facing the world today. Hg^{2+} is one of the most dangerous pollutants in heavy metals. Due to the high toxicity and bioaccumulation of mercury, it has a serious impact on biology and the environment.[1,2] Hg^{2+} can cause serious damage to various organs in the body, and even affect the immune system.[3] Aluminum is the most abundant metal elements in the crust, and there are many aluminum products in life, such as cooking utensils, aluminum containers and so on. This will lead to increased levels of Al^{3+} in the environment, and its slow accumulation in the human body will affect human health, in particular the brain, liver, heart and bone marrow.[4–6] Therefore, the qualitative and quantitative detection of Hg^{2+} and Al^{3+} is very meaningful. However, the traditional detection methods include absorption spectroscopy and inductively coupled plasma mass spectrometry. However, due to the complex operation, long time-consuming and high cost, people have developed a variety of sensor platform systems, among which the carbon quantum dot fluorescent probe is one. Because of its simple operation, rapid analysis, high selectivity and high sensitivity, it has attracted people's attention.[7]

Cucurbit[*n*]urils (Q[*n*]s) are spherical macrocyclic compounds adopting a stable rigid structure, and are composed of *n* glycoluril units bridged by 2*n* methylene groups with a hydrophobic cavity. The cavity can vary in size, but possesses two polar carbonyl ports with negative electrostatic potential.[8–10] Given the presence of the rigid cavity and carbonyl port, Q[*n*]s exhibit excellent affinity for metal ions and protonated alkylamines through hydrophobic interactions and ion-dipole interactions.[11,12] Q[*n*]s with different sizes of internal cavity and carbonyl-based ports shows excellent molecular recognition function in aqueous solution,[13,14] which has seen Q[*n*]s become an ideal choice for optical sensors and molecular switches. Indeed, they are now widely used in sensing, drug delivery, nanomaterials and other fields.[15–19] However, several inherent disadvantages of Q[*n*]s hinder their wider development and application. Firstly, Q[*n*]s do not possess any absorption or fluorescence in the visible region. Secondly, Q[*n*]s homologues have poor solubility in pure water and in most common organic solvents. Thirdly, Q[*n*]s homologues are difficult to functionalize and therefore modify. As a result, it is necessary to introduce new concepts and methodologies to further improve the properties of the Q[*n*]s.[20,21]

Carbon quantum dots (CQDs) are the latest members of the fluorescent carbon nano-sized family. CQDs have been recognized as discrete quasi-spherical particles with sizes below 10 nm.[22–24] Due to their biocompatibility, low toxicity, excellent photostability, good water solubility and easy functionalization, CQDs have been widely used in food and environment-related ion detection, bioimaging, drug delivery, cancer treatment and other fields.[25–28] So far, however, the luminescence mechanism of carbon quantum dots remains unclear. Studies have shown that the emission characteristics of CQDs are highly dependent

[a] *Key Laboratory of Macrocyclic and Supramolecular Chemistry of Guizhou Province, Guizhou University, Guiyang 550025, China. E-mail: zengxi1962@163.Com*
[b] *Public Course Teaching Department, Qiannan Medical College for Nationalities, Duyun, 558000, China*
[c] *Department of Chemistry, University of Hull, Hull HU6 7RX, UK. E-mail: c.redshaw@hull.ac.uk*

† Electronic supplementary information (ESI) available. See DOI: 10.1039/d2qm00022a

on the size of the CQD core and the type of surface functional groups present.[29] The size of the Q[*n*]s varies with the n value, and on combining with CQDs, it is expected that CQDs with different particle sizes and luminescent properties will be afforded. The excellent water solubility and easy functionalization of carbon quantum dots make up for many of the shortcomings of the cucurbituril ring systems. Therefore, we have combined the preparation technology of carbon quantum dots with the cucurbit[*n*]urils structure to prepare a new class of carbon quantum dots.

Q[7]-CQDs and Q[8]-CQDs have been synthesized by hydrothermal methods using Q[*n*]s (n = 7, 8). Results showed that the framework of the Q[*n*]s remained intact during this process, and the obtained Q[*n*]-CQDs (n = 7, 8) were shown to be potential multicolor biomarkers according to cytotoxicity tests and cell imaging results.[30] In this paper, based on the previous large particle sizes of Q[7] and Q[8], this study has used a single Q[6] with a smaller particle size as the precursor, and phenylenediamine (*o*-phenylenediamine, *m*-phenylenediamine, *p*-phenylenediamine) as the doping reagent. Through a one-step hydrothermal synthesis, N and O groups with hydrophilic and recognition functions on the surface of CQDs were directly obtained. Carbon quantum dots (*m*-Q[6]-CQDs) formed from Q[6] and *m*-phenylenediamine were studied. Compared with Q[7]-CQDs and Q[8]-CQDs, *m*-Q[6]-CQDs showed better light stability and salt tolerance. Meanwhile, *m*-Q[6]-CQDs can specifically recognize Hg^{2+} and Al^{3+} and allow for optical bioimaging to be performed on human prostate cancer (PC-3) cells; excellent selectivity and sensitivity to Hg^{2+} and Al^{3+} and impressive cell imaging ability are revealed.

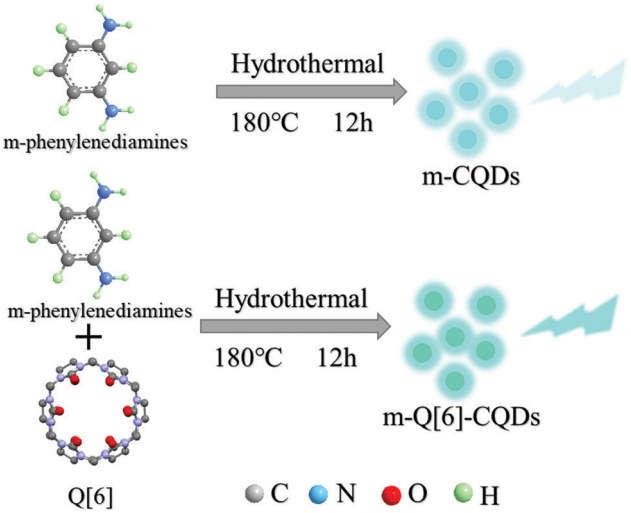

Fig. 1 Preparation of *m*-CQDs and *m*-Q[6]-CQDs.

2. Result and discussion

In this paper, three new Q[6]-CQDs (*o*-Q[6]-CQDs, *m*-Q[6]-CQDs, *p*-Q[6]-CQDs) were synthesized by solvothermal methods using Q[6] and phenylenediamine (*o*-phenylenediamine, *m*-phenylenediamine, *p*-phenylenediamine) as raw materials. Due to the weak brightness of *o*-Q[6]-CQDs and *p*-Q[6]-CQDs under UV, they are not ideal. This paper mainly studies the properties of *m*-Q[6]-CQDs. Following work-up (see experimental section), the *m*-Q[6]-CQDs were isolated in moderate yield (23%). The structure and morphology of the *m*-Q[6]-CQDs were characterized by a series of experiments, and the crystal structure of the *m*-Q[6]-CQDs was determined by an X-ray powder diffraction experiment. As shown in Fig. 1a, there is an obvious diffraction peak at about 24.6°, corresponding to (002) of hexagonal graphite, which indicates that the prepared carbon quantum dots have a complete and continuous crystal structure, with an sp^2 hybrid carbon core and an sp^3 hybrid carbon shell of graphite carbon. The *m*-Q[6]-CQDs were further characterized by Fourier transform infrared spectroscopy (FTIR, see Fig. 1b), where the broad absorption peak at 3440 cm^{-1} is attributed to the stretching vibrations of ν_{O-H} and ν_{N-H}, whilst that at 2924 cm^{-1} and 2854 cm^{-1} belong to the stretching vibration of C–H. A peak at 1740 cm^{-1} corresponds to the stretching vibration of C=O, whilst 1327 cm^{-1} belongs to the stretching vibration peak of C–N. Peaks at 1636 cm^{-1} are assigned to a C=C stretching

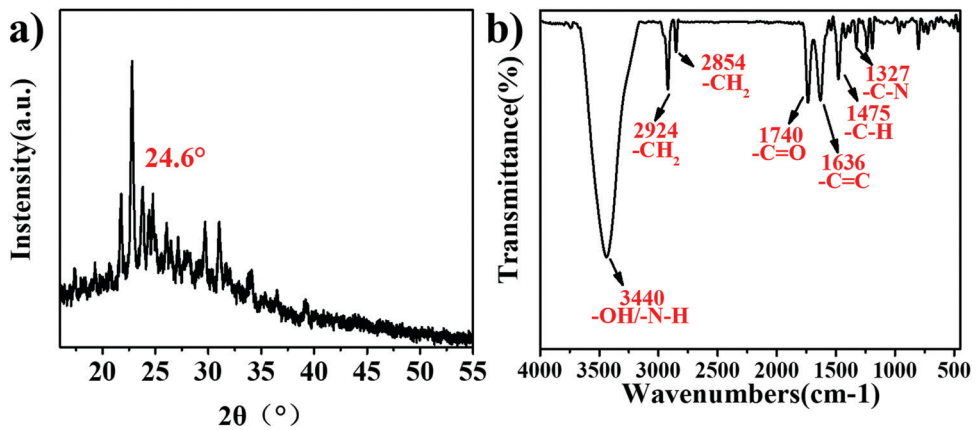

Fig. 2 (a) XRD characterization; (b) infrared spectrum of the *m*-Q[6]-CQDs.

vibration, and the bending vibration of aromatic C–H, The N–H bond, C═C bond and aromatic C–H bond in the infrared spectrum can preliminarily determine that the *m*-Q[6]-CQDs were successfully synthesized.

The morphology of the synthesized *m*-Q[6]-CQDs was recorded by high-resolution transmission electron microscopy (HRTEM) (Production method, ESI† S1). As shown in Fig. 2, the synthesized carbon dots are spherical and uniformly dispersed without aggregation, and the average particle size is about 3.2 nm. The illustration shows that there is an ordered lattice structure on the surface of the *m*-Q[6]-CQDs observed under high resolution transmission electron microscopy (HRTEM). The crystal plane spacing is about 0.208 nm, which corresponds to the (100) plane of the hexagonal lattice in the graphite carbon plane. This is consistent with the formation of a graphitized structure within the *m*-Q[6]-CQDs. On comparing Q[7]-CQDs with Q[8]-CQDs, Q[7]-CQDs had better dispersibility due to the high solubility of Q[7], so the measured average particle size was small. The properties of Q[6] and Q[8] are similar, and the size of Q[8] is larger than Q[6], so the average particle size of *m*-Q[6]-CQDs is smaller than Q[8]-CQDs, which is consistent with the experimental results.

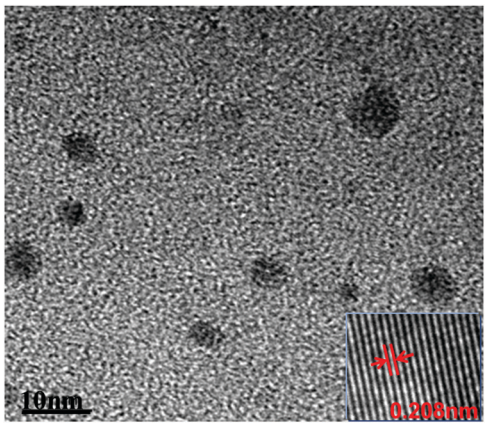

Fig. 3 HRTEM imaging of *m*-Q[6]-CQDs.

The chemical composition of the *m*-Q[6]-CQDs was determined by X-ray photoelectron spectroscopy. Fig. 3a shows clear peaks of C 1s, O 1s and N 1s, and the samples were located at 285.07, 532.10 and 399.94 eV, respectively, indicating that the samples were mainly composed of C, O and N elements. Higher C and O content confirmed that the *m*-Q[6]-CQDs are rich in oxygen-containing functional groups. Fig. 3b shows the fine spectrum of C 1s, and the absorptions at 285.03 eV, 287.5 eV and 289.1 eV, which indicate the existence of C–C/C═C, C–N and C═O bonds, respectively. In the N 1s spectra, absorptions at 399.4, 400.3 and 401.8 eV can be attributed to C–N, N–H and N–O bonds, respectively. In the case of the O 1s spectra, absorptions at 531.98 and 533.67 eV correspond to C═O and C–OH bonds, respectively. Due to the existence of C═C, N–H,

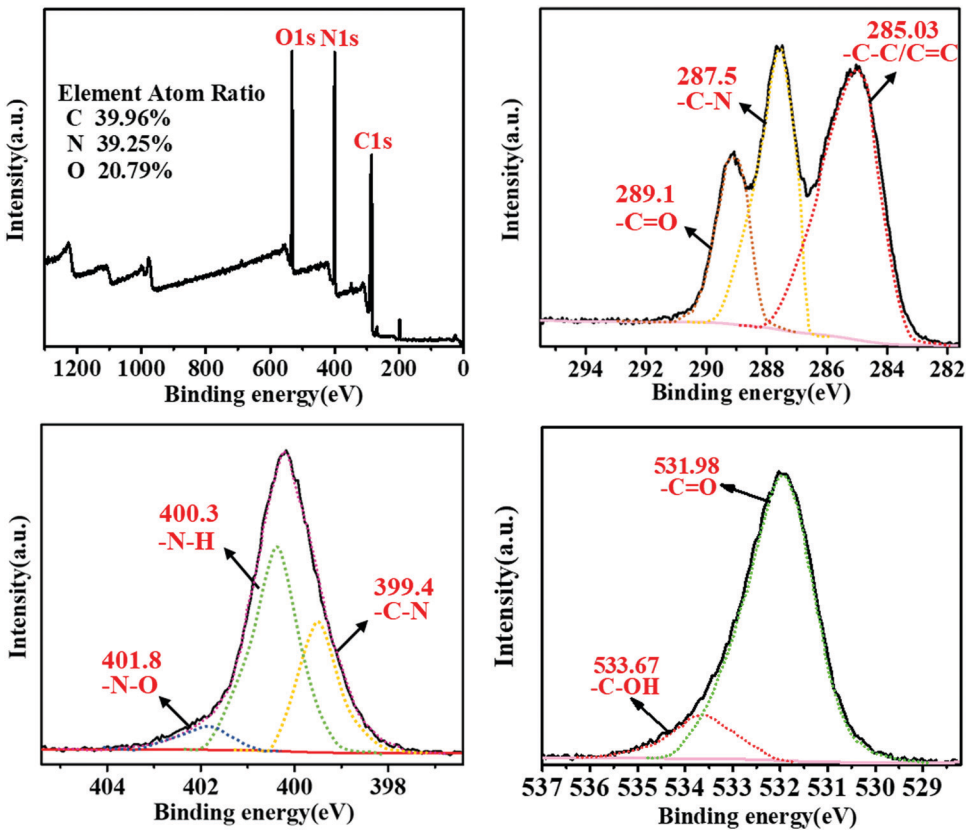

Fig. 4 (a) XPS spectra of *m*-Q[6]-CQDs; (b, c and d) high resolution spectra of C 1s, N 1s and O 1s, respectively.

C–OH bonds, it was further verified that *m*-Q[6]-CQDs were successfully synthesized. The presence of these hydrophilic functional groups enhances the water solubility and stability of the *m*-Q[6]-CQDs, thereby making the *m*-Q[6]-CQDs highly dispersed and stable in aqueous solution. Interestingly, compared with Q[6]-CQDs and *m*-CQDs, the ratio of N in *m*-Q[6]-CQDs increased significantly. The nitrogen content gradually increased from 28.91% of Q[6]-CQDs and 20.20% of *m*-CQDs to 39.25% of *m*-Q[6]-CQDs, and the oxygen content increased from 18.90% of Q[6]-CQDs and 5.60% of *m*-CQDs to 20.79% of *m*-Q[6]-CQDs. In addition, the carbon content decreased from 52.20% of Q[6]-CQDs and 74.20% of *m*-CQDs to 39.96% of *m*-Q[6]-CQDs. These results indicate that Q[6]-CQDs and *m*-CQDs are mainly composed of C, while *m*-Q[6]-CQDs are mainly composed of N and O doped carbon. In essence, the changes of the C, N and O components in the *m*-Q[6]-CQDs are mainly attributed to the effective catalytic fusion and carbonization of *m*-phenylenediamine by the portal in Q[6].

Fig. 4A shows the optical images of the fluorescence spectra and UV absorption spectra of the *m*-Q[6]-CQDs (solution preparation, ESI† S1). The *m*-Q[6]-CQDs have a characteristic absorption peak at 285 nm, which is attributed to the n–π * transition of the C=O bond. Under excitation at 385 nm, the maximum emission of the *m*-Q[6]-CQDs is at 485 nm. The *m*-Q[6]-CQDs solution is light yellow under natural light and emits bright green fluorescence under UV light (365 nm). Fig. 4B shows that the fluorescence intensity of the *m*-Q[6]-CQDs changes with the excitation wavelength. When the excitation wavelength changes from 365 nm to 465 nm, the emission intensity of the *m*-Q[6]-CQDs gradually decreases and the emission peak shifts to the red. This red shift is related to the narrow size distribution and surface passivation function of the *m*-Q[6]-CQDs. Therefore, *m*-Q[6]-CQDs with blue-green fluorescence have been successfully prepared.

The prepared *m*-Q[6]-CQDs exhibited good stability, and the fluorescence intensity of the *m*-Q[6]-CQDs did not change significantly in different concentrations of NaCl solution (solution preparation, ESI† S1). Indeed, *m*-Q[6]-CQDs can remain stable for at least two hours in high ionic strength solutions. As shown in Fig. 5a, the *m*-Q[6]-CQDs can be stored stably for more than two months in a refrigerator at 4 °C. This suggests that the use of these *m*-Q[6]-CQDs as fluorescent probes to detect targets in complex matrixes has great application prospects. The effect of pH on the *m*-Q[6]-CQDs was investigated as shown in Fig. 5b. The strong fluorescence emission under acidic conditions may be due to the protonation of the carbonyl, amino or C=N functions at the surface of, or internal to, the *m*-Q[6]-CQDs. The fluorescence intensity of these functional groups decreased sharply under the

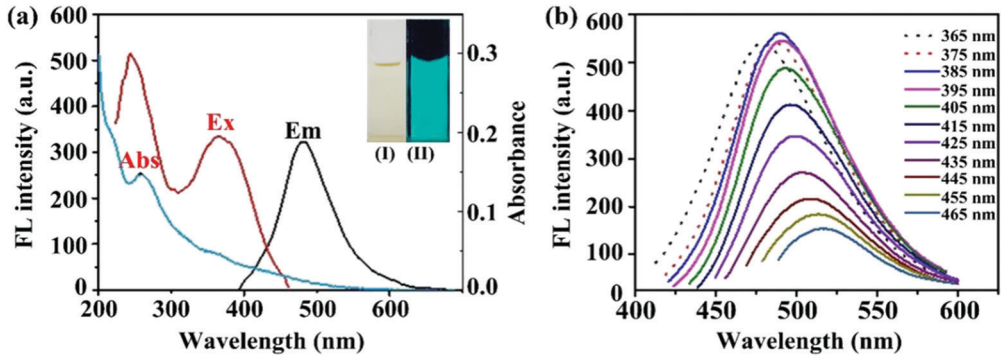

Fig. 5 (a) UV absorption spectrum and emission spectrum of the *m*-Q[6]-CQDs. The illustrations are the optical images of *m*-Q[6]-CQDs solution (i) under natural light irradiation and (ii) ultraviolet lamp irradiation; (b) fluorescence emission spectra of *m*-Q[6]-CQDs at excitation wavelengths of 365–465. The solvent used is ultrapure water.

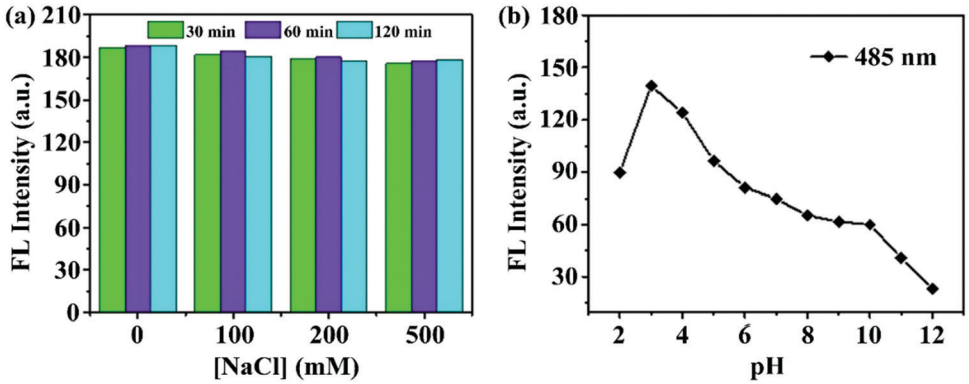

Fig. 6 (a) The effect of ionic strength on the fluorescence intensity of the *m*-Q[6]-CQDs; (b) the effect of pH on the fluorescence intensity of the *m*-Q[6]-CQDs; the *m*-Q[6]-CQDs concentration was 0.1 mg mL^{-1}, $\lambda_{ex}/\lambda_{em}$ = 385/485 nm. The solvent used is ultrapure water.

action of deprotonation, and the strong acidic environment tended to saturate the protonation of the functional groups of the *m*-Q[6]-CQDs, and so the fluorescence intensity would not increase under a strongly acidic environment.

We then investigated whether the interaction of the *m*-Q[6]-CQDs and *m*-CQDs with common metal ions (Al^{3+}, Fe^{3+}, Ca^{2+}, Cd^{2+}, Co^{2+}, Cu^{2+}, Hg^{2+}, Mg^{2+}, Mn^{2+}, Ni^{2+}, Pb^{2+}, Zn^{2+}, Ag^{+}, Na^{+}, K^{+}) would affect the fluorescence intensity of the *m*-Q[6]-CQDs (solution preparation, ESI† S1). As shown in Fig. 6a, Hg^{2+} can quench the fluorescence of the *m*-Q[6]-CQDs, whilst Al^{3+} slightly enhanced the fluorescence of the *m*-Q[6]-CQDs. *m*-CQDs were only selective to Hg^{2+}, which reduced the fluorescence intensity, while the interaction between *m*-CQDs and Al^{3+} remained almost unchanged (ESI† S6). Fig. 6b presents the infrared spectrum of the *m*-Q[6]-CQDs and contrasts it with the spectra after adding mercury ions or aluminium ions. The peaks at 3440 cm^{-1} and 2924 cm^{-1} are assigned to the stretching vibrations of O–H/N–H. The peak at 1740 cm^{-1} corresponds to the stretching vibration of C=O, whilst that at 1475 cm^{-1} belongs to the bending vibration of C–N. Other peaks include

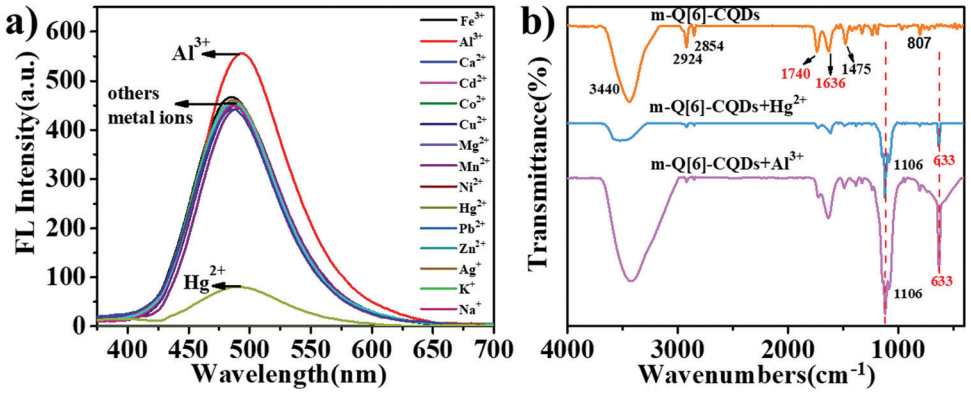

Fig. 7 (a) Interaction of the *m*-Q[6]-CQDs with different metal ions under neutral conditions, the *m*-Q[6]-CQDs concentration is 0.38 mg mL^{-1}, $\lambda_{ex}/\lambda_{em}$ = 385/485 nm; (b) comparison of the infrared spectra of the *m*-Q[6]-CQDs with Hg^{2+} and Al^{3+}. The concentration of all metal ions is 0.2 mM. The solvent used is ultrapure water.

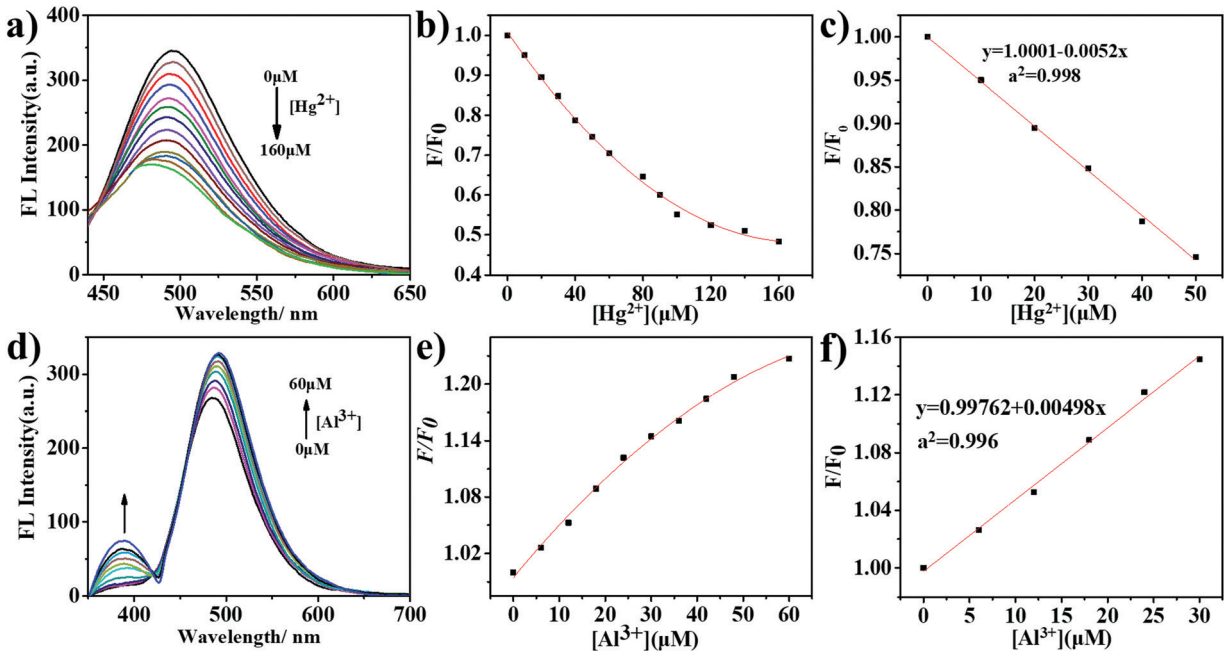

Fig. 8 (a) Spectral changes of the *m*-Q[6]-CQDs solution containing different concentrations of mercury ions; (b and c) the linear curve between the fluorescence quenching efficiency of the *m*-Q[6]-CQDs and the concentration of mercury ions. The illustration shows that the fluorescence quenching efficiency is proportional to the concentration of mercury ions over the range 0–50 μM. The pH of the PBS buffer = 6.5. The excitation wavelength is 385 nm; (d) spectra of the *m*-Q[6]-CQDs solution containing different concentrations of aluminium ions; (e and f) the linear curve between the fluorescence quenching efficiency of *m*-Q[6]-CQDs and the concentration of aluminium ions. The illustration shows that the fluorescence quenching efficiency is proportional to the concentration of mercury ions over the range 0–30 μM. The pH of the PBS buffer is 6.5, the concentration of *m*-Q[6]-CQDs is 0.19 mg mL^{-1}, and $\lambda_{ex}/\lambda_{em}$ = 385/485 nm. The solvent used is ultrapure water.

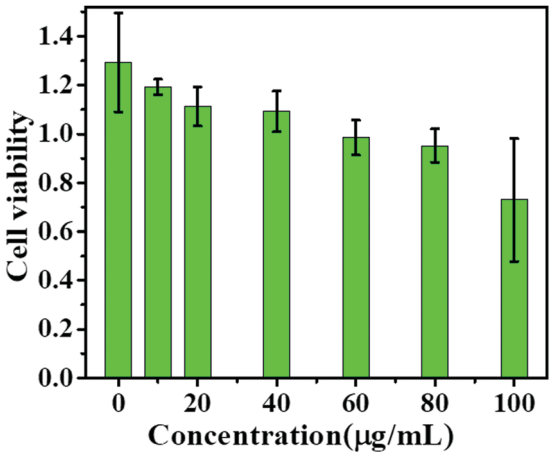

Fig. 9 Toxicity experiment of *m*-Q[6]-CQDs on PC-3 cells.

the stretching vibration of C=C at 1636 cm^{-1}, and the out-of-plane bending vibration of aromatic C–H at 807 cm^{-1}. After the addition of Hg^{2+} and Al^{3+}, two new peaks appeared at 1106 cm^{-1} and 633 cm^{-1}, indicating the interaction between metal ions (Hg^{2+}, Al^{3+}) and *m*-Q[6]-CQDs.

We then added different concentrations of Hg^{2+} and Al^{3+} to the *m*-Q[6]-CQDs solution to study the change of fluorescence intensity (solution preparation, ESI† S1). As shown in Fig. 7a, on increasing the mercury ion concentration from 0 to 160 μM, the fluorescence intensity of the *m*-Q[6]-CQDs at 485 nm gradually decreased. Fig. 7b shows that the concentration of Hg^{2+} and fluorescence quenching efficiency are linear over the range 0 to 50 μM. In the figure, C refers to the concentration of Hg^{2+}, F_0 and F represent the fluorescence intensity of the *m*-Q[6]-CQDs in the absence and presence of Hg^{2+}, respectively. According to the signal-to-noise ratio formula S/N = 3, the detection limit (LOD) is 0.4 μM. Fig. 7d shows that when the concentration of Al^{3+} increases from 0 to 60 μM, the fluorescence intensity of the *m*-Q[6]-CQDs at 385 nm and 490 nm gradually increases. Fig. 7e shows that the concentration of Al^{3+} and the fluorescence quenching efficiency are linear over the range 0 to 30 μM, and the detection limit is 0.2 μM according to the same method. At the same time, we also studied the fluorescence intensity change of the *m*-CQDs solution with different concentrations of Hg^{2+} (ESI† S6). When the Hg^{2+} concentration increased from 0 to 20 μM, the fluorescence intensity of *m*-CQDs at 485 nm gradually decreased. The linear range was 0–20 μM, and the detection limit was 1.2 μM. The quantum yields of *m*-CQDs and *m*-Q[6]-CQDs are 0.41% and 2.34%, respectively. The quantum yields of *m*-Q[6]-CQDs interacting with Hg^{2+} and Al^{3+} are 1.39% and 2.88%, respectively. The quantum yields of *m*-CQDs interacting with Hg^{2+} and Al^{3+} are 0.18% and 0.44%, respectively. It can be seen from the detection limit and quantum yield that the introduction of Q[6] into *m*-CQDs not only increases the fluorescence intensity and quantum yield of the CQDs, but also results in a smaller detection limit for Hg^{2+}. Therefore, *m*-Q[6]-CQDs have better optical properties than *m*-CQDs.

In this study, human prostate cancer (PC-3) cells were used as an example to determine the cytotoxicity of the *m*-Q[6]-CQDs by CCK-8 assay. A CCK-8 assay showed that these *m*-Q[6]-CQDs displayed low cytotoxicity at 0–80 μg mL^{-1} and acted as a bioimaging reagent (Fig. 8) (experimental process, ESI† S1). In addition, it was also found from these images that the *m*-Q[6]-CQDs are mainly located in the nuclear region. The *m*-Q[6]-CQDs were applied to the cell imaging of human hepatocellular carcinoma PC-3 cells (Fig. 10). The *m*-Q[6]-CQDs were diluted to a certain concentration and used for labeling of PC-3 cells. The fluorescence images of the cells obtained by a fluorescence inverted microscope were used for labeling (Fig. 9). The above results indicated that the *m*-Q[6]-CQDs had successfully entered the living cells and maintained good fluorescence properties within the cells. At the same time, the fluorescence of the *m*-Q[6]-CQDs was quenched following the addition of mercury ions.

3. Conclusions

In this study, we have synthesized new *m*-Q[6]-CQDs *via* the use of solvothermal synthesis, and the *m*-Q[6]-CQDs product has been characterized by a variety of techniques including FTIR, XRD and X-ray photoelectron spectroscopy. The *m*-Q[6]-CQDs exhibit good stability, and the fluorescence intensity is maintained in highly ionic solutions for two hours. The effect of pH

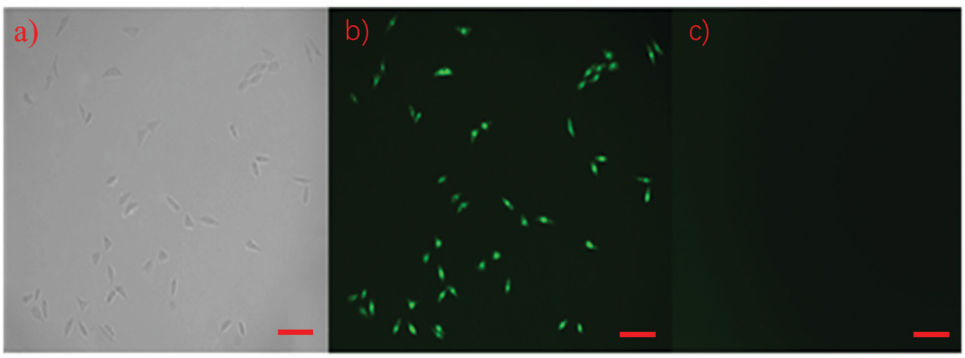

Fig. 10 PC-3 cells were incubated with *m*-Q[6]-CQDs (50 μg mL^{-1}), (a) and photographed in tomorrow; (b) imaging map under GFP457 channel; (c) photographs of fluorescence quenching of pc-3 cells after adding mercury ion solution, [Hg^{2+}] = 50 μM. The scale bar represents 60 μm.

was examined and acidic conditions were found to be most favourable for fluorescence intensity. It was also demonstrated that the fluorescence of *m*-Q[6]-CQDs is resistant of the interference of metal ions, and the high ionic strength environments. High selectivity and sensitivity to Hg^{2+} and Al^{3+} was revealed in aqueous solution, and the Hg^{2+} was found to quench fluorescence, whilst Al^{3+} slightly enhanced the fluorescence. Since Hg^{2+} and Al^{3+} can cause serious damage to various organs *in vivo*, the qualitative and quantitative detection of Hg^{2+} is of great significance for biological research. This behavior, combined with the low cytotoxicity properties, suggest that these *m*-Q[6]-CQDs have potential as an excellent fluorescent probe for use in cellular imaging.

Conflicts of interest

The authors declare no competing financial interest.

Acknowledgements

We thank the Innovation Program for High-level Talents of Guizhou Province (No. 2016-5657) are gratefully acknowledged for financial support and the Science and Technology Fund of Guizhou Province ([2020]1Y051). CR thanks the EPSRC for an Overseas Travel Grant (EP/R023816/1).

Notes and references

1 C. Yang, Y. Li, N. Wu, Y. Zhang, W. Feng, M. Yu and Z. Li, Ratiometric upconversion luminescence nanoprobes for quick sensing of Hg^{2+} and cells imaging, *Sens. Actuators, B*, 2021, **326**, 128841, DOI: 10.1016/j.snb.2020.128841.

2 E. M. Nolan and S. J. Lippard, Tools and tactics for the optical detection of mercuric ion, *Chem. Rev.*, 2008, **108**, 3443–3480, DOI: 10.1002/chin.200850280.

3 X. Zhao, S. Campbell, P. Z. El-Khoury, Y. Jia, G. Q. Wallace, A. Claing, C. G. Bazuin and J.-F. Masson, Surface-Enhanced Raman Scattering Optophysiology Nanofibers for the Detection of Heavy Metals in Single Breast Cancer Cells, *ACS Sens.*, 2021, **6**, 1649–1662, DOI: 10.1021/acssensors.1c00332.

4 J. Zhu, H. Chu, T. Wang, C. Wang and Y. Wei, Fluorescent probe-based nitrogen doped carbon quantum dots with solid-state fluorescence for the detection of Hg2+ and Fe3+ in aqueous solution, *Microchem. J.*, 2020, **158**, 105142, DOI: 10.1016/j.microc.2020.105142.

5 G. Berthon, Aluminium speciation in relation to aluminium bioavailability, metabolism and toxicity, *Coord. Chem. Rev.*, 2002, **228**, 319–341, DOI: 10.1016/S0010-8545(02)00021-8.

6 P. Nayak, Aluminum: Impacts and Disease, *Environ. Res.*, 2002, **89**, 101–115, DOI: 10.1006/enrs.2002.4352.

7 W. Wei, J. Huang, W. Gao, X. Lu and X. Shi, Carbon Dots Fluorescence-Based Colorimetric Sensor for Sensitive Detection of Aluminum Ions with a Smartphone, *Microchem. J.*, 2021, **9**, 25, DOI: 10.3390/chemosensors9020025.

8 N.-N. Li, M. Yang, X.-J. Xu, X.-Y. Dong, S. Li and S.-Q. Zang, Ensembles from silver clusters and cucurbit[6]uril-containing linkers, *Dalton Trans.*, 2021, **50**, 15267–15273, DOI: 10.1039/d1dt02505h.

9 K. O. Ramberg, S. Engilberge, F. Guagnini and P. B. Crowley, Protein recognition by cucurbit[6]uril: high affinity N-terminal complexation, *Org. Biomol. Chem.*, 2021, **19**, 837–844, DOI: 10.1039/d0ob02356f.

10 F.-F. Shen, K. Chen, Y.-Q. Zhang, Q.-J. Zhu, Z. Tao and H. Cong, Mono- and Dihydroxylated Symmetrical Octamethylcucurbiturils and Allylated Derivatives, *Org. Lett.*, 2016, **18**, 5544–5547, DOI: 10.1021/acs.orglett.6b02789.

11 Y. Meng, W. Zhao, J. Zheng, D. Jiang, J. Gao, Y. Jin and P. Ma, Host–guest modes and supramolecular frameworks of complexes of tetramethyl cucurbit[6]uril with 4-chloroaniline and 4,4′-diaminostilbene, *RSC Adv.*, 2021, **11**, 3470–3475, DOI: 10.1039/D0RA09074C.

12 S. Sin and F. Biedermann, Chemical Sensors Based on Cucurbit[n]uril Macrocycles, *Isr. J. Chem.*, 2018, **58**, 357–412, DOI: 10.1002/ijch.201700118.

13 S. J. Barrow, S. Kasera, M. J. Rowland, J. D. Barrio and O. A. Scherman, Cucurbituril-Based Molecular Recognition, *Chem. Rev.*, 2015, **115**, 12320–12406, DOI: 10.1021/acs.chemrev.5b00341.

14 G. Ghale and W. M. Nau, Dynamically Analyte-Responsive Macrocyclic Host-Fluorophore Systems, *Acc. Chem. Res.*, 2014, **47**, 2150–2159, DOI: 10.1021/ar500116d.

15 G. Cheng, J. Luo, Y. Liu, X. Chen and T. Chen, Cucurbituril-Oriented Nanoplatforms in Biomedical Applications, *ACS Appl. Bio Mater.*, 2020, **3**, 8211–8240, DOI: 10.1021/acsabm.0c01061.

16 L. You, D. Zha and E. V. Anslyn, Recent Advances in Supramolecular Analytical Chemistry Using Optical Sensing, *Chem. Rev.*, 2015, **115**, 7840–7892, DOI: 10.1021/acsabm.0c01061.

17 T. Wang, Y. Tang, X. He, J. Yan, C. Wang and X. Feng, *ACS Appl. Mater. Interfaces*, 2017, **9**, 6902–6907.

18 I. Ghosh and W. M. Nau, The strategic use of supramolecular pKa shifts to enhance the bioavailability of drugs, *Adv. Drug Delivery Rev.*, 2012, **64**, 764–783, DOI: 10.1016/j.addr.2012.01.015.

19 E. A. Pashkina, L. V. Grishina, A. A. Aktanova and V. A. Kozlov, Antitumor activity of supramolecular complexes of cucurbituril with platinum (II) compounds, *Inorg. Chim. Acta*, 2021, **522**, 120370, DOI: 10.1016/j.ica.2021.120370.

20 R. H. Gao, L. X. Chen, K. Chen, Z. Tao and X. Xiao, Development of hydroxylated cucurbit[n]urils, their derivatives and potential applications, *Coord. Chem. Rev.*, 2017, **348**, 1–24, DOI: 10.1016/j.ccr.2017.07.017.

21 S. Sinn and F. Biedermann, Chemical Sensors Based on Cucurbit[n]uril Macrocycles, *Isr. J. Chem.*, 2018, **58**, 357–412, DOI: 10.1002/ijch.201700118.

22 A. Sharma and J. Das, Small molecules derived carbon dots: synthesis and applications in sensing, catalysis, imaging, and biomedicine, *J. Nanobiotechnol.*, 2019, **17**, 92, DOI: 10.1186/s12951-019-0525-8.

23 T. Medeiros, J. Manioudakis, F. Noun, J. R. Macairan and R. Naccache, Microwave-Assisted Synthesis of Carbon Dots

and Their Applications, *J. Mater. Chem. C*, 2019, **7**, 7175–7195, DOI: 10.1039/C9TC01640F.

24 R. Prasad, D. S. Chauhan, A. S. Yadav, J. Devrukhkar, B. Singh, M. Gorain, M. Temgire, J. Bellare, G. C. Kundu and R. Srivastava, A biodegradable fluorescent nanohybrid for photo-driven tumor diagnosis and tumor growth inhibition, *Nanoscale*, 2018, **10**, 19082–19091, DOI: 10.1039/C8NR05164J.

25 H. Jin, E. S. Feura and M. H. Schoenfisch, Theranostic Activity of Nitric Oxide-Releasing Carbon Quantum Dots, *Bioconjugate Chem.*, 2021, **32**, 367–375, DOI: 10.1021/acs.bioconjchem.1c00002.

26 N. Zhao, J. Song, Z. Huang, X. Yang, Y. Wang and L. Zhao, Ratiometric fluorescence probe of Cu^{2+} and biothiols by using carbon dots and copper nanoclusters, *RSC Adv.*, 2021, **11**, 33662–33674, DOI: 10.1039/dira05854a.

27 Gunture, J. Kaushik, D. Saini, R. Singh, P. Dubey and S. K. Sonkar, Surface adhered fluorescent carbon dots extracted from the harmful diesel soot for sensing Fe(III) and Hg(II) ions, *New J. Chem.*, 2021, **45**, 20164–20172, DOI: 10.1039/D1NJ04189D.

28 J. Wan, X. Zhang, K. Fu, X. Zhang, L. Shang and Z. Su, Highly fluorescent carbon dots as novel theranostic agents for biomedical applications, *Nanoscale*, 2021, **13**, 17236–17253, DOI: 10.1039/d1nr03740d.

29 B. Yao, H. Huang, Y. Liu and Z. Kang, Carbon dots: A Small Conundrum, *Trends Chem.*, 2019, **1**, 235–246, DOI: 10.1016/j.trechm.2019.02.003.

30 S. Cao, P. Wang, X. Zeng, Z. Tao and X.-L. Ni, Cucurbituril-assisted formation of tunable carbon dots from single organic precursors in water, *Org. Chem. Front.*, 2021, **8**, 224–230, DOI: 10.1039/D0QO01143F.

